

PCCP

Accepted Manuscript



This is an *Accepted Manuscript*, which has been through the Royal Society of Chemistry peer review process and has been accepted for publication.

Accepted Manuscripts are published online shortly after acceptance, before technical editing, formatting and proof reading. Using this free service, authors can make their results available to the community, in citable form, before we publish the edited article. We will replace this *Accepted Manuscript* with the edited and formatted *Advance Article* as soon as it is available.

You can find more information about *Accepted Manuscripts* in the [Information for Authors](#).

Please note that technical editing may introduce minor changes to the text and/or graphics, which may alter content. The journal's standard [Terms & Conditions](#) and the [Ethical guidelines](#) still apply. In no event shall the Royal Society of Chemistry be held responsible for any errors or omissions in this *Accepted Manuscript* or any consequences arising from the use of any information it contains.

Spectroscopy of Discrete Vertically Oriented Single-Crystals of N-Type Tetraazaterrylene: Understanding the Role of Defects in Molecular Semiconductor Photovoltaics

Cite this: DOI: 10.1039/x0xx00000x

Received 00th January 2012,
Accepted 00th January 2012

DOI: 10.1039/x0xx00000x

www.rsc.org/

A.J. Wise,^a Y. Zhang,^b J. Fan,^c F. Wudl^c, A.L. Briseno^b and M.D. Barnes^{a*}

Recent synthetic work has realized a novel (n-type) small-molecule acceptor, 7,8,15,16-Tetraaza-terrylene (TAT), single-crystals of which can be grown oriented along the c-axis crystallographic direction, and over-coated with pentacene to form a highly ordered donor/acceptor interface for use in organic photovoltaic devices. However, characterization of single TAT crystals reveals highly variable emission spectra and excited state dynamics – properties which strongly influence photovoltaic performance. Through the use of single-crystal widefield imaging, photoluminescence spectroscopy, time correlated single photon counting, and resonant Raman studies, we conclude that this variability is a result of long-lived low-energy trap-emission from packing defects. Interestingly, we also discovered that TAT crystals whose width exceeds ~200 nm begin acting as waveguides and optical microcavity resonators for their own photoluminescence. Several strategies are proposed for leveraging the size-dependant optical properties of TAT pillars to further enhance device performance using this active layer design.

^a Dept. of Chemistry, University of Massachusetts, Amherst MA.

^b Dept. of Polymer Science, University of Massachusetts, Amherst MA.

^c Dept. of Chemistry, University of California, Santa Barbara

1. Introduction

As a result of their photo-stability and high fluorescence quantum yield, the Rylene family of dyes has attracted enormous interest in a variety of applications including fluorescent labeling in biological systems,¹ light-emitting diodes (LED)², transistors,³ and organic photovoltaic (OPV) applications,^{4,5} as well as a platform for probing fundamental photophysics associated with chromophore-chromophore interactions. Frontier orbital energy levels can be readily controlled by extending the molecule lengthwise or by

addition of functional groups to the central ‘bay’ regions.⁶ Due to the facility with which they can be tuned, Rylenes are a natural basis for the formation of supramolecular structures,⁷ including donor acceptor dyads,^{8,9} dimers,¹⁰ trimers,¹¹ and dendrimers¹² with engineered structures and aggregate wave functions. Terrylene diimide (TDI) has previously been investigated as an electron acceptor material for use in a P3HT/TDI photovoltaic blend.¹³ However, as in other bulk heterojunction active layer designs, gross phase segregation appears to limit power conversion efficiency. This is often a difficulty with polymer/small molecule blends as annealing, even the small amount that occurs during drying after the initial film formation, can form a heterogeneous and difficult to characterize interface. Imposition of desirable interface geometry,

whether by templating or controlled crystal growth, seeks to avoid the temperamental nature of the spontaneously formed bulk heterojunction interface.

Recently, a nitrogen-substituted terrylene analogue, 7,8,15,16-Tetraazaterrylene (TAT), has been synthesized,¹⁴ and subsequently used to form nanostructured photovoltaic active layers. TAT is of particular interest due to its ability to form high-density, vertically oriented nanopillars on graphene, which can be backfilled with an appropriate hole acceptor material to generate an ultra-high surface area, yet highly crystalline, heterojunction. This architecture is predicted to become a target for several different synthetic approaches as a geometry for which charge separation and extraction is expected to be optimal,¹⁵ yet is only weakly approximated by traditional bulk heterojunctions formed by spinodal spontaneous demixing. We recently developed a technique for growing vertically oriented single crystals with tunable areal density via physical vapor deposition on a variety of substrates such as graphene, PEDOT, and other conventional electrode substrates.

TAT crystals were prepared using a modified thermal deposition technique whereby vertically oriented single-crystal pillars grow from a graphene substrate. Nanopillar dimensions are controlled by deposition rate and time; the full details of the growth process are discussed elsewhere. Growth onto a graphene substrate followed by deposition of a pentacene donor layer results in a functional photovoltaic device, while growth of TAT nano- and micro-pillars on the inner wall of a quartz tube results in more heterogeneous crystals which can be used to understand crystal growth and photophysics in this material. We used single-particle spectroscopy on isolated TAT nanopillars to investigate how size and morphology impacts optical properties relevant to OPV device performance. With a combination of wavelength, time, and polarization resolved photoluminescence, we identify low energy

states created by crystallographic packing defects as a loss mechanism that competes with exciton dissociation, and the competition between pristine excitonic and defect-related emission. Further, we observed the spectroscopic signatures of optical microcavity resonance and waveguiding from the pillar end facets in larger (diameter $\geq \lambda_{\text{PL}}/2$) TAT pillars.

2. Experimental Details

2.1 Optical measurements:

Absorption spectra of thin films were recorded on a Shimadzu UV-3600. Steady state photoluminescence measurements were carried out on home-built confocal/widefield microscope/spectrometer system based around a Nikon TE300 microscope body. Widefield PL images were recorded via a trinocular-mounted Princeton ProEM-512 CCD. Spectra were recorded with an Acton SP2150 spectrometer equipped an 600 line/mm (blaze 500nm) grating with a Princeton PIXIS CCD. Excitation for photoluminescence spectra was provided by the 514nm line of a Spectra Physics 163-CO₂ argon-ion laser, although no shape in PL spectra between 405nm and 532nm excitation was apparent. Typical excitation intensities were $\sim 250 \text{ W cm}^{-1}$, with no measureable photobleaching over the course of any measurements. Excitation for TCSPC measurements was provided by a Picoquant LDH-405 405nm diode laser, and timing recorded by routing the output of a ID-Quantique ID100 avalanche photodiode into a PicoHarp 300 TCSPC module. Wavelength-resolved TCSPC measurements were recorded by mounting the detector at the exit port of the spectrometer.

2.2 Crystal Growth

Tetraazaterrylene (TAT) was previously synthesized and

described in a previous publication.¹⁴ The process of horizontal physical vapor transport was used to grow TAT single-crystals on single-layer graphene substrates. To deposit the crystals, we placed the receiving graphene substrate 6 centimeters away from the source material in a perpendicular orientation to the flow direction of crystallization. Approximately 10 mg of TAT was placed inside the tube at the hottest temperature zone, which was held at a constant temperature of ~ 370 °C. Subsequently, the tube furnace was kept under a vacuum pressure of ~ 0.45 mTorr using a standard laboratory vacuum pump. Vertically oriented TAT single crystals were grown in 14 min. Bulk quantities of TAT crystals were also grown on the inside of glass sleeves at a reduced pressure of $\sim 10^{-4}$ mBar. The crystals are grown in about 8-10 minutes and subsequently harvested manually.

3. Results & Discussion

Figure 1 shows the crystal structure of TAT. To correlate the molecular packing of molecules to the morphology of a TAT crystal, we carried out transmission electron microscope (TEM) diffraction on a single crystal. The results indicate that molecules crystallize in a 1-D face-on packing motif along the [100] growth direction (Fig. 1b). The molecular packing is shown as an overlay on the single crystal in Figure 1b. The reciprocal diffraction spots show a geometry consistent with the bulk monoclinic unit cell of TAT where, $a = 3.7429$ Å, $b = 15.815$ Å, $c = 13.990$ Å, $\alpha = 90.00^\circ$, $\beta = 93.947^\circ$, $\gamma = 90.00^\circ$.

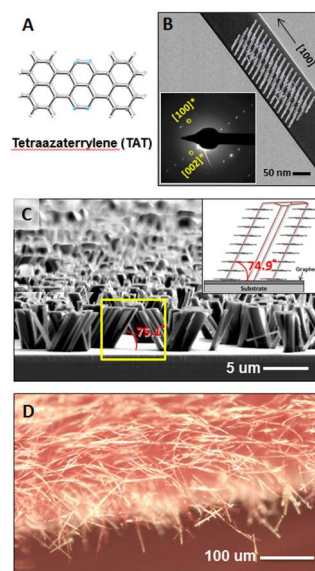


Figure 1. A) Chemical structure of tetraazaterrylene (TAT). B) TEM image and corresponding electron diffraction pattern (inset) from a single-crystal TAT nanopillar. The diffraction spots indicate that the growth direction of the crystalline pillar is along the [100] (i.e., the unit cell a-axis). C) Scanning electron microscope (SEM) image of vertically oriented TAT pillars on graphene. The inset shows the theoretically predicted growth morphology of a TAT single crystal. The tilt angle (74.9°) between packing of flat-lying molecules and the basal plane closely equals that of bulk pillars observed from SEM (75.1°). D) Optical microscope image (illuminated under dark-field conditions) of a network of TAT ultralong nanowires grown in a glass sleeve.

Growth of TAT pillars on a graphene substrates typically result in a densely-packed array of vertically oriented nanostructures - a geometry which provides high surface area when backfilled with a hole-accepting (e.g. pentacene) layer. The morphology of vertically oriented pillars grown on graphene substrates is shown in Figure 1c by scanning electron microscopy (SEM). From the crystal habit of TAT pillars shown in Figure 1c, the calculated tilt angle is 75.1° . This value is consistent with the tilt angle of 74.9° in the crystal structure (shown as inset in Fig 1c). Polycyclic aromatic hydrocarbons (PAHs) are known to self-assemble via strong π - π

interactions, which lead to the formation of one-dimensional (1D) structures. Grazing incidence x-ray diffraction (GIXD) experiments indicate that TAT nanopillars grow from the graphene surface with the plane of the molecule parallel to the surface of the substrate – an orientation which favors efficient charge transport through the device (see **figure S6**). In fact, a very similar packing has been demonstrated by perylene-3,4,9,10-tetracarboxylic dianhydride (PTCDA) directly onto graphene via epitaxial self-assembly.¹⁶ This was also demonstrated by DFT-based *ab initio* calculation methods.¹⁷ Figure 1d shows an optical image of TAT nanowires grown directly onto glass sleeves by a fast rate of deposition which yields high-aspect ratio crystals.

One of the attractive features of the TAT system is the relatively broad and low-energy absorption spectrum that facilitates efficient capture of solar energy; when combined with a pentacene donor layer, the absorption extends further into the near infra-red.

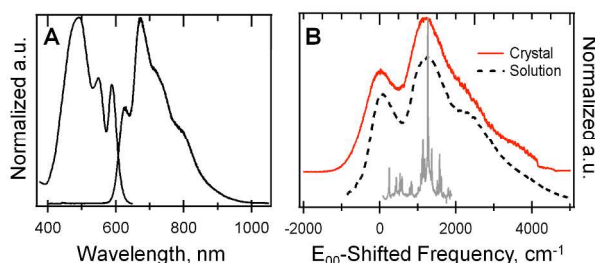


Figure 2. A) Ensemble UV/VIS absorption and PL spectra of slowly grown, high quality TAT crystals, revealing an apparently high Huang-Rhys factor (>1) relative to unsubstituted terryelene (not shown, ~ 0.3). B) origin-shifted PL spectra of a single TAT nanocrystal (solid trace) and TAT dissolved in chloroform (dashed). The lack of significant change in PL envelope shape from solution to solid state is consistent with extremely weak intermolecular electronic coupling within the TAT crystal. Overlaid is the resonant Raman spectrum (514nm excitation) in the fingerprint region, demonstrating that the spectral envelope is energetically consistent with a high-displacement vibronic progression rather than some more exotic effect.

Figure 2 shows the absorption and PL emission spectrum (2a) of an ensemble of high quality, slow grown TAT nanopillars. Surprisingly, PL spectra of TAT nanopillars and chloroform-solvated TAT (figure 2b, solid and dashed traces, respectively) show nearly identical vibronic sideband intensity ratios, suggesting that the weak 0-0/0-1 ratio is the result of high electron-phonon coupling (Huang-Rhys Factor > 1) rather than aggregate dipole interactions, e.g. weak H-coupling. Although there is a significant gas to crystal shift, $\sim 2180\text{cm}^{-1}$, the lack of significant change in the emission envelope is surprising when compared to other rylene. Again, we attribute this to weak coupling between neighboring TAT molecules within the crystal.

The TAT emission spectrum appears at first glance as a low-displacement vibronic spectrum with E_{00} at 680nm and an odd shoulder at 640nm. However, the spacing of vibronic sidebands corresponds with the frequency of coupled vibrational modes in the molecule. If the emission spectra are shifted by the electronic origin (E_{00}) energy, the spacing between vibronic replicas approximates the mean frequency of the principally-displaced vibrational modes present in the resonant Raman spectrum ($\lambda_{\text{exc}}=514\text{nm}$, overlaid in figure 2b), supporting the identification of the emission envelope as a high-displacement vibronic spectrum intrinsically broadened by the participation of >10 vibrational modes over a wide frequency range.

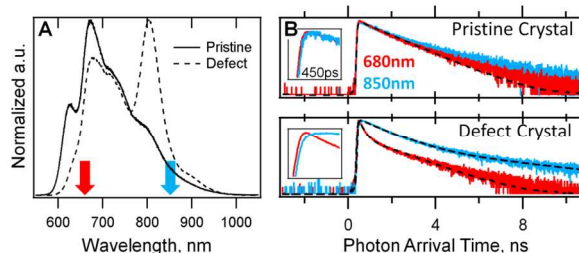


Figure 3. A) PL spectra of a single TAT crystal grown slowly ($<1\text{mm}$

length/min, solid line) compared with a quickly grown crystal (>2mm length/min, dashed lined). Fast pillar growth causes the emergence of a new emission band centered at 800nm, likely due to crystallographic defects. B) Wavelength and time resolved PL measurements of the pristine slow grown crystal (top) and defect-ridden fast grown crystal (bottom) show clear changes in emission dynamics. Pristine crystals show single-exponential decay kinetics ($t = 1.1$ ns fit, dashed line) at both 680nm (red) and 850nm (blue). Emission in the defective crystals shifts to bi-exponential decay at 680nm ($t_1 = 0.16$ ns, $t_2 = 1.1$ ns), while the defect-specific band at 850nm displays a second slower emitter ($t_1 = 0.97$ ns, $t_2 = 3.9$ ns) and significant differences in rise dynamics (first 450ps inset) indicative of energy transfer.

While PL emission from slowly-grown crystals differs little from solvated molecules, increasing the growth rate of TAT crystals, whether by fast vapor deposition onto glass sleeves or slower deposition directly onto graphene, results in extreme changes in the nature of intermolecular coupling. The emission spectra of fast-grown TAT crystals is shown in Figure 3, contrasted against similar size crystals grown more slowly, but under otherwise similar conditions and from the same starting material. Dissolving these ‘defective’ TAT crystals in chloroform recovers an emission spectrum identical to that shown in figure 2b, suggesting that this ‘defect’ emission is not due to fluorescent impurities or bulk chemical change of the TAT, e.g. due to oxidation.

Wavelength resolved time-correlated single photon counting (TCSPC) measurements (figure 3b) reveal a significantly longer excited state lifetime for this ‘defect’ emission band relative to the pristine TAT emission, indicating a separate emission mechanism. Close examination of the TCSPC signal (3b, inset) shows that the ‘defect’ emission band rises slowly relative to the pristine crystal vibronic emission – a consequence of indirect population via trapping after absorption. As transfer to the trap

state is accompanied by an energy loss of ≈ 0.22 eV, subsequent hole transfer to pentacene can no longer proceed spontaneously - The addition of a pentacene hole-acceptor does not result in quenching of the ‘defect’ state (see figure S1). Consequently, trapping by defect states in TAT acts a potentially large loss mechanism in devices with defect-dense crystals. High efficiency nanostructured solar cells require tremendous attention to growth and structure of the constituent structures to achieve high performance.

Analogous phenomena are observed in nominally single-crystal rubrene samples: high quality, slowly grown crystals luminescence with a single vibronic progression ($\lambda_{\text{max}} = 615$ nm), while those with packing defects feature a second, red shifted vibronic progression ($\lambda_{\text{max}} = 650$ nm).¹⁸ This defect-associated emission band has been variously attributed to recombination of triplet excitons in amorphous inclusions,¹⁸ vibronic sideband emission from a single electronic origin,¹⁹ and uncorrected self-absorption and polarization measurement artifacts.²⁰ Both TAT and rubrene crystals display few of the spectral signatures of aggregation, representing a class of organic crystals with a notable lack of the spectroscopic signatures of aggregation. Thus, we expect our observations here to contribute to a general understanding of photophysical processes in this class of materials rather than insights unique to TAT.

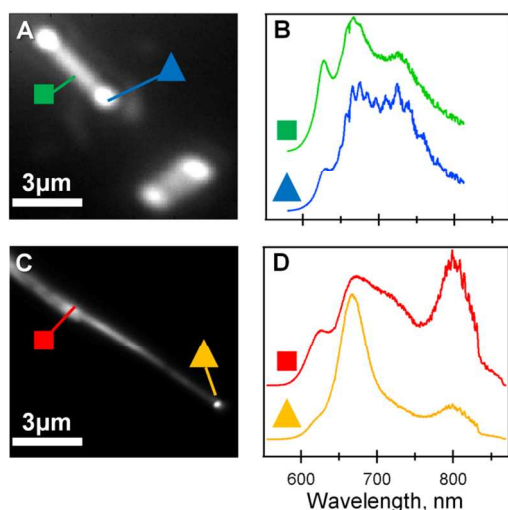


Figure 4. *A) Wide field PL image of small slowly-grown TAT crystals, showing enhanced emission at both ends due to wave guiding. B) Spatially-resolved emission spectra, showing unperturbed emission from the body of the crystal, while emission from the ends of the crystal display an interference pattern consistent with a micron-scale 1D optical resonator, and attenuated 0-0 emission due to self-absorption during propagation along the long axis. C) Wide-field PL image of a fast-grown TAT crystal with a twin-like defect. Spatially resolved PL (D), shows typical defective crystal emission from the body (dominated by the 800nm band) and narrowed end emission due to self-absorption and wavelength-dependent waveguide transmission efficiency.*

Wide field PL microscopy of single TAT nano-pillars (Figure 4 a,c) reveals interesting relationships between size, shape, crystal quality, and optical properties. Single slow-grown crystalline TAT nanopillars are shown in figure 4a. Under wide field 514nm excitation, emission from the central region of the crystal is similar to the ‘pristine’ crystal PL spectrum shown in figure 2b. However, spatially resolved PL from either end of the crystal shows attenuated 0-0 emission and a periodic envelope modulation with a frequency of $\sim 360\text{cm}^{-1}$. These features are with the result of wave guiding of PL along the crystal body between reflective terminal facets – with the entire pillar forming a single-crystal optical resonator. The

oblique end facets of the slowly-grown crystals, as seen in figure 2a, complicate analysis of the exact resonator mode structure, but the spacing seen here is roughly consistent with the trivial case of a cylindrical crystal of several microns in length. The attenuated 0-0 emission is due to self-absorption losses during propagation along the waveguide, as the small Stokes shift results in significant overlap of the 0-0 emission and absorption bands.

In contrast, a single ‘defective’ fast-grown TAT nanopillar is shown in figure 4a. Spatially-resolved emission spectra from an apparent twinning defect (4d, square marker) shows dominant ‘defect band’ emission centered at 800 nm, while the pillar apex (4d, triangle marker) shows weak defect emission but drastically enhanced pristine vibronic emission centered at 650 nm. Polarization-resolved PL measurements from this structure (figure S2) demonstrate the approximate co-linearity of the sample plane projection of the emission dipoles of both emissive species – indicating that the ‘defect’ emission is not orthogonal to ‘pristine’ vibronic emission, and likely due to horizontally adjacent molecules rather than between π -stacked neighbors. Interestingly, the PL spectrum of quaterrylene (the larger homologue of terrylene) is also centered at 800 nm, devoid of visible vibronic features, and of approximately the same width.²¹

Spatially resolved emission from the ‘defective’ pillar shown in figure 4b appears to show significant PL narrowing, with strong enhancement of the 0-1 emission band, relative to the 0-2 band, with almost complete suppression of the 0-0 origin. This would be consistent with a stimulated emission (SE) or amplified spontaneous emission (ASE) process, by which early PL guided along the pillar growth axis radiatively dumps excitonic emission further down the TAT crystal long axis. Stimulated emission in organic materials generally results in enhanced 0-0 (pure electronic) emission and extremely narrow line widths, as is the case for heavily

studied p-sexiphenyl nanofibers.²² The enhancement of the 0-1 emission here would be explained by consideration of a lack of significant gain at the 0-0 energy due to strong self absorption of PL.

However, while the structure shown in figure 4a is an optimal geometry for generating stimulated emission, we have generally not observed stimulated or amplified spontaneous emission in these structure, with pulsed and continuous-wave excitation yielding virtually identical emission envelopes despite a >1000-fold increase in peak power (see figure S3). This is likely a result of weak reflection at the crystal end facets combined with a relatively low PL quantum yield in the material ($h \ll 0.1$). Yet, in pillars like that in 4c, funneling of PL from the entire $\approx 15\mu\text{m}$ pillar along a gradually-narrowing body to a $\approx 1/2$ diameter apex undoubtedly concentrates the guided wave's energy and provides the potential for nonlinear optical processes to occur. The spectra shown in 4d – specifically the strong attenuation of the 0-0 transition and relative enhancement of the 0-1 transition) are difficult to explain without invoking stimulated or amplified spontaneous emission, but this not a general property of TAT crystals and is likely dependent on particularly favorable crystallite geometries. Further studies correlating atomic force microscopy sizing measurements and optical properties are currently underway.

Although unsuitable for direct use in OPV devices, one interesting aspect of the 'defective' TAT pillars is their demonstration of surprising spatial heterogeneity of optical properties over extremely small regions. Single pillars no longer than a few hundred nanometers can display markedly different properties at opposite ends, which demands rigorous characterization of size-structure-property relationships before efficient and reliable devices can be built from these interesting nanocrystalline components. **Figure 5** shows two overlapping, highly heterogeneous TAT pillars, with wavelength- and polarization-resolved

measurements that provide insight into the source of long-lived trap emission band at 800 nm.

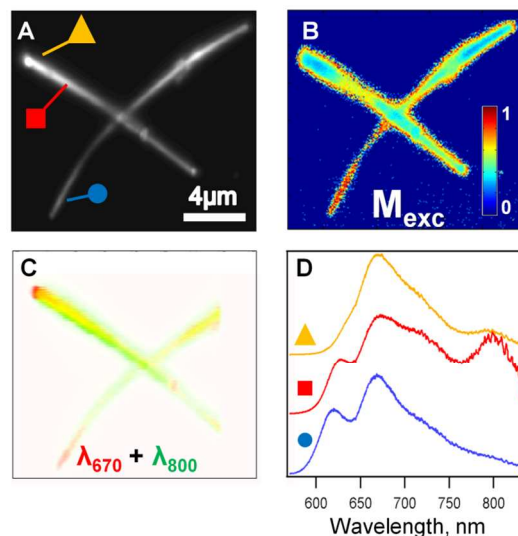


Figure 5. Heterogeneity within single TAT pillars. *A)* Wide field PL image of two highly heterogeneous fast-grown TAT pillars. *B)* Spatially-resolved PL, from regions marked in *A*. Emission from the non-narrowing crystal face at the upper left (orange triangle) shows strong wave guiding, while the region at lower left (blue circle) shows a return to pristine-type emission with no apparent wave guiding or self absorption. Hyperspectral imaging of these structures (*C*) shows regions with 'pristine'-dominant (red), defect-dominant (green) or mixed (yellow) emission spectra. Photoluminescence-detected linear excitation anisotropy shown in *D* reveals a very high anisotropy (approaching 1) in regions with pristine-type emission, and low anisotropy in defect-heavy regions.

Figure 5a (top left), shows a relatively large and bright pillar that terminates in a waveguide-active end. At bottom left, a much thinner crystal narrows into a nearly diffraction-limited pillar with no measureable waveguide emission. Photoluminescence spectra from the regions indicated by markers (5d) show enhanced 0-1 emission from the waveguide-active apex (square) and strong defect emission from the large pillar body (triangle). However, the

relatively thin fiber (circle) displays an emission envelope similar to that shown in figure 2b and discussed above – similar to slowly grown high quality TAT pillars. A false-color wide field hyperspectral PL image (5c) shows the relative intensity of the pristine crystal exciton emission (peak 670nm) relative to that of the ‘defect’ band (800nm). This measurement reveals a clear shading to green (pristine crystal vibronic emission) along the length of the narrower fiber. The larger fiber (top left to bottom right) shows dominant defect emission along the entire length, with a small spot of red at the fiber apex due to PL waveguided along the growth axis and scattered into the detector by the substrate and defects at the pillar end facet.

Figure 5b shows a per-pixel excitation anisotropy generated by rotation of the polarization plane of the excitation source. The excitation anisotropy M is calculated from the minimum and maximum PL intensities I_{\min} and I_{\max} via equation 1.

$$M_{exc} = \frac{I_{\max} - I_{\min}}{I_{\max} + I_{\min}} \quad (1)$$

There is a clear correspondence between the false-color wide field PL and anisotropy – with defect-dominant regions of the cluster featuring significantly lower anisotropy values. In contrast, the smaller, exciton-dominant fiber at lower right has an anisotropy approaching 1, indicating a single direction of molecular alignment. Based on these observations, we conclude that the source of the excimer-like emission is the introduction of defects into the TAT crystal structure, due to growing-together of multiple pillars or direct formation of twinning defects during rapid growth. We believe the collinearity (at least in the projection of the sample plane) of the excimer and exciton emission dipole rule out the defect emission as a result of widespread random defects, which would result in unpolarized defect emission. However, we are not currently able to

definitively describe this state, and use the term ‘defect’ out of convenience rather than conviction. Further study of this system, especially TEM studies of highly defective crystals, will help elucidate the nature of these defects. As well, better understanding of the possible participation of otherwise-silent excited states²³ and a more complete prediction of exciton coupling between neighboring molecules in any potential allotropes²⁴ will allow a more fundamental understanding of the limitations and potential of this material.

4. Conclusions

Our investigation of the growth-dependent photophysical properties of TAT nanopillars both in ensemble and as single crystals/wires has provided interesting new insights into their function in OPV devices. Pristine TAT nanocrystals behave spectroscopically like isolated single molecules, indicating weak electronic coupling between nearest neighbors and implying a short exciton diffusion radius. Under highly controlled growth conditions, TAT single-crystals can be grown many microns in length without perturbing the electronic structure. However, at higher growth rates we observed the formation of a relatively long-lived low-energy defect state that manifests as a near-IR emission band, competing with charge separation at the donor/acceptor interface. This state could potentially be quenched by a lower-gap hole acceptor and would potentially result in efficiency gains in defect-heavy devices – the 1.5eV gap of the defect trap state is still significantly above that of silicon and certainly worth harvesting.

The similarities between the ‘defect’ emission band of TAT and emission from quaterylene, the higher homologue of terrylene – namely, nearly identical energy and emission envelope shape – lead us to tentatively identify this band as emission from

excitations delocalized over two neighboring slip-stacked TAT molecules. Continued work is underway to better understand the origin of the defect state. An additional surprising feature of the TAT nano/micro pillar system is that for pillars wider than $\lambda_{\text{PL}}/2$, optical waveguiding of the intra-crystal PL is observed. While these pillars are too large to use in a high surface area nanoscale heterojunction, the apparent low stimulated emission threshold in some geometries and directed emission raises intriguing possibilities for a waveguide-based solar cell. Currently, we are attempting to leverage this emissive process as a way to funnel energy collected along the entire pillar to a localized site for charge separation by depositing a cap of quenching material on the pillar apex. This would allow efficient long-range shuttling of excitations over long distances, and remove the limitations imposed by weakly mobile thermally relaxed excited states

Acknowledgements

MDB and AJW acknowledge support from US Department of Energy under Grant # DE-FG02-05ER15695 (Program Manager: Larry Rahn). JF was supported by the Center for Energy Efficient Materials, an Energy Frontier Research Center funded by the U.S. Department of Energy, Office of Science, Office of Basic Energy Sciences under Award Number DE-SC0001009 and Department of Energy (grant no. DE-FG02-08ER46535). A.L.B acknowledges support by the Office of Naval Research (N000141110636).

Notes and references

Electronic Supplementary Information (ESI) available: Photoluminescence quenching measurements of the TAT/pentacene blends, polarization-resolved photoluminescence measurements of single TAT crystals, photoluminescence of individual crystals under pulsed and

continuous-wave excitation, experimental schema for widefield hyperspectral imaging and crystal growth, and GIXD patterns for vertically oriented TAT nanocrystals. See DOI: 10.1039/b000000x/

1. T. Weil, T. Vosch, J. Hofkens, K. Peneva, and K. Müllen, *Angew. Chem. Int. Ed.*, 2010, **49**, 9068–9093.
2. C. Ego, D. Marsitzky, S. Becker, J. Zhang, A. C. Grimsdale, K. Müllen, J. D. MacKenzie, C. Silva, and R. H. Friend, *J. Am. Chem. Soc.*, 2003, **125**, 437–443.
3. A. L. Briseno, S. C. B. Mannsfeld, C. Reese, J. M. Hancock, Y. Xiong, S. A. Jenekhe, Z. Bao, and Y. Xia, *Nano Lett.*, 2007, **7**, 2847–2853.
4. U. B. Cappel, A. L. Smeigh, S. Plogmaker, E. M. J. Johansson, H. Rensmo, L. Hammarström, A. Hagfeldt, and G. Boschloo, *J. Phys. Chem. C*, 2011, **115**, 4345–4358.
5. X. Zhan, A. Facchetti, S. Barlow, T. J. Marks, M. A. Ratner, M. R. Wasielewski, and S. R. Marder, *Adv. Mater. Weinheim*, 2011, **23**, 268–284.
6. Q. Bai, B. Gao, Q. Ai, Y. Wu, and X. Ba, *Org. Lett.*, 2011, **13**, 6484–6487.
7. F. Würthner, *Chem. Commun.*, 2004, 1564.
8. H. N. Kim, L. Puhl, F. Nolde, C. Li, L. Chen, T. Basché, and K. Müllen, *Chemistry*, 2013, **19**, 9160–9166.
9. G. Hinze, R. Métivier, F. Nolde, K. Mullen, and T. Basché, *J Chem Phys*, 2008, **128**, 124516.
10. A. Issac, R. Hildner, D. Ernst, C. Hippus, F. Würthner, and J. Köhler, *Physical Chemistry Chemical Physics*, 2012, **14**, 10789–10798.
11. J. Hernando, J. Hoogenboom, E. van Dijk, J. García-López, M. Crego-Calama, D. Reinhoudt, N. van Hulst, and M. García-Parajó, *Phys. Rev. Lett.*, 2004, **93**, 236404.
12. M. Sliwa, C. Flors, I. Oesterling, and J. Hotta, *Journal of Physics: ...*, 2007.
13. J. Gorenflot, A. Sperlich, A. Baumann, D. Rauh, A. Vasilev, C. Li, M. Baumgarten, C. Deibel, and V. Dyakonov, *Synthetic Metals*, 2012, **161**, 2669–2676.
14. J. Fan, L. Zhang, A. L. Briseno, and F. Wudl, *Org. Lett.*, 2012.

15. Y. Wei, C. Xu, S. Xu, C. Li, W. Wu, and Z. L. Wang, *Nano Lett.*, 2010, **10**, 2092–2096.
16. Q. H. Wang and M. C. Hersam, *Nature Chem.*, 2009, **1**, 206–211.
17. X. Q. Tian, J. B. Xu, and X. M. Wang, *J. Phys. Chem. C*, 2010, **114**, 20917–20924.
18. Y. Chen, B. Lee, D. Fu, and V. Podzorov, *Adv. Mater.*, 2011, **23**, 5370–5375.
19. X. Wen, P. Yu, C.-T. Yuan, X. Ma, and J. Tang, *J. Phys. Chem. C*, 2013, **117**, 17741–17747.
20. P. Irkhin, A. Ryznyanskiy, M. Koehler, and I. Biaggio, *Phys. Rev. B*, 2012, **86**, 085143.
21. S. K. Lee, Y. Zu, A. Herrmann, Y. Geerts, K. Müllen, and A. J. Bard, *J. Am. Chem. Soc.*, 1999, **121**, 3513–3520.
22. H. Yanagi, T. Ohara, and T. Morikawa, *Adv. Mater.*, 2001.
23. S. Tavazzi, A. Borghesi, A. Papagni, P. Spearman, L. Silvestri, A. Yassar, A. Camposeo, M. Polo, and D. Pisignano, *Phys. Rev. B*, 2007, **75**, 245416.
24. S.-H. Lim, T. Bjorklund, F. Spano, and C. Bardeen, *Phys. Rev. Lett.*, 2004, **92**, 107402.